Ytterbium-Doped Glass Waveguide Laser Fabricated by Ion Exchange

Catalin Florea, *Student Member, IEEE, Member, OSA*, and Kim A. Winick, *Senior Member, IEEE, Member, OSA*

Abstract—A ytterbium-doped, glass, channel waveguide laser, fabricated by ion exchange, is reported. The 2.2-cm long device, using broad-band 4% output couplers, lased in the vicinity from 1020 to 1030 nm when pumped by a Ti : sapphire laser operating at 910 nm. A lasing threshold of 50 mW (launched pump) and a slope efficiency of 5% were measured. Device parameters, including fluorescence lifetimes, emission and absorption cross sections, propagation losses, and mode profiles were experimentally determined and laser performance was analytically modeled using this data.

Index Terms—Integrated optics, ion exchange, waveguide laser, ytterbium laser.

I. INTRODUCTION

$Yb3^+$ ions in glass and crystals have a number of important properties, which make these laser materials of practical interest. The Yb^{3+} energy level structure is particularly simple, consisting of a ground state manifold, $^2F_{7/2}$, Stark-split into four sublevels and a excited-state manifold, $^2F_{5/2}$, Stark-split into three sublevels. Thus, excited state absorption(ESA) at both the pump and signal wavelengths, is absent. The upper manifold lies approximately $10\,500$ cm^{-1} above the ground level [1]. This large energy gap precludes significant multiphonon nonradiative decay [2], and the broad absorption spectrum, due to Stark-splitting, permits a wide choice of pump wavelengths. Finally, the broad emission spectrum of this material and its large saturation fluence permits lasing to be achieved over a wide range of wavelengths (1–1.2 μm)^3 and makes it an attractive medium for the generation and amplification of ultrashort pulses [4], [5]. Applications of Yb^{3+} lasers include (1) 1020 nm pumps for 1300 nm fiber amplifiers [6] and upconversion lasers in praseodymium-doped ZBLAN^7, (2) 1140 nm pumps for thulium-doped ZBLAN upconversion lasers [8], (3) 1083 nm narrow-line sources for the spectroscopic study of helium [9], and (4) amplifiers for ultrashort pulses [5]. In addition Yb^{3+} has been widely used as a sensitizer for Er^{3+}-doped glass amplifiers and lasers [10]. In such devices, a cooperative cross-relaxation process between Yb^{3+} and Er^{3+} ions allows the $^4I_{13/2}$ level of Er^{3+} to be efficiently populated when pumping on the $^2F_{7/2} \rightarrow ^2F_{5/2}$ transition of Yb^{3+}.

The first report of Yb^{3+} lasing was by Etzel, Gandy, and Ginther in 1962 for a lithium-magnesium alumino-silicate glass rod, which was cooled to 77 K and flashlamp-pumped [11]. Oscillation was obtained at 1015 nm. Laser action was subsequently demonstrated in several other Yb^{3+}-doped, bulk, glass [12] and crystal hosts [13]. These results were extended to Yb^{3+}-doped, silica, fiber lasers by Hanna *et al.* in 1988 [14]. The fiber geometry is ideally suited to applications which require, robust, compact devices and/or low pump power thresholds. Tunable operation [15], operation in fluoride hosts [16], fiber laser cavities with intracore distributed Bragg reflectors [17] and distributed feedback gratings [18], and short-pulse generation using stretched-pulse techniques [4] were also reported in Yb^{3+}-doped fibers in recent years. A review of ytterbium-doped, silica, fiber lasers up to 1994, was prepared and published by Pask *et al.* in 1995 [3]. Ytterbium-doped fiber amplifiers have also been developed [5], [19], [20].

Planar waveguide geometries, as opposed to fibers, allow multiple components to be integrated on a single substrate. In addition, higher doping levels (and shorter devices) can be realized, since a larger variety of glass hosts can be utilized. A broad range of rare earth-doped, waveguide amplifiers and lasers have been previously reported in glasses and crystals [21]. Yb^{3+}-doped, planar, waveguide lasers have been fabricated in YAG by epitaxial growth [22] and by ion implantation [23]. Yb^{3+}-doped, channel, waveguide lasers have also been reported in gadolinium gallium garnet [24] and lithium niobate [25]. In addition, low-power, all-optical, switching devices have been demonstrated in Yb^{3+}-doped optical fibers [26] and planar waveguides [27] based on pump-induced resonant nonlinearities at 1301 and 1545 nm.

This paper reports (to the best of our knowledge) the first demonstration of a Yb^{3+}-doped channel waveguide laser in a glass host. The 2.2-cm long device was fabricated by potassium ion exchange in a sodium-rich, multicomponent, silicate glass, which contained 12 wt% Yb_2O_3. The parameters of the devices, including fluorescence lifetimes, emission and absorption cross sections, propagation losses, and mode profiles were experimentally determined and laser performance was modeled using this data.

The remainder of this paper is organized as follows. In Section II the spectroscopy of the Yb^{3+} ions in the sodium-rich, multicomponent, silicate glass is reported. In particular, the positions of the Stark split energy levels are estimated from measured absorption and fluorescence data, and a McCumber analysis is used to compute the emission cross section. The fluorescence lifetime is also measured. In Section III, the ion exchange process is described, and waveguide loss measurements and mode profiles are reported together with laser

TABLE I
Yb-Doped Glass Composition

compound	weight percentage
SiO_2	67.7
NaO_2	12.5
K_2O	3.53
BaO	4.08
Yb_2O_3	12

performance. Modeling results are presented in Section IV and compared with the experimental data of the previous section. The laser model developed in Section IV takes into account the pump and signal mode profiles and is based on a set of standard rate equations combined with a Rigrod analysis. Our conclusions are presented in Section V.

II. SPECTROSCOPY

The coordination of Yb^{3+} in several inorganic glasses was studied using low temperature optical absorption and fluorescence spectra by Robinson and Fournier [1], [28]. The Yb^{3+} ion has a $^4f_{13}$ ground state configuration which gives rise to the mulitplet $^2F_{7/2}$, $^2F_{5/2}$, with the former lying at the lowest energy level. The two J levels are separated by approximately $10\,500$ cm^{-1}, and each are Stark-split by interaction with the local crystal fields at the rare earth sites. The lower and upper levels are split into four and three nondegenerate sublevels, respectively. Absorption and fluorescence data are consistent with Yb^{3+} ions located at sites of nearly octahedral symmetry with six-fold coordination. The alkali-barium-silicate glass used in our device had the composition shown in Table I.

At 633 and 830 nm, the measured refractive indexes of the glass were 1.5136 and 1.5083, respectively. Room-temperature absorption data taken with a spectrophotometer allowed us to clearly resolve absorption peaks at 972, 958, and 906 nm (see Fig. 2). Fluorescence data taken at 77 K with 960 nm pumping allowed us to resolve two strong emission peaks at 972 and 1005 nm. Two smaller peaks, which were barely observable, were estimated to lie at 1062 and 1016 nm, respectively. The fluorescence signal was collected using a geometry with the pump and the detector located on the same side of the glass sample, and the pump focused very close to the glass surface. This geometry minimized possible reabsorption of the fluorescence signal. At room temperature emission was also seen in the vicinity of 470–550, 655–672, and 355 nm. These peaks are consistent with trace thulium contamination of the Yb_2O_3 reagent from which the glass was melted. The energy level diagram shown in Fig. 1 was derived from our measured emission and absorption spectra. This diagram is quite similar to that reported in [1] for a alkali-barium-silicate glass of a slightly different composition. The emission cross section, σ_e, was derived from absorption spectra using the McCumber analysis [29], [30] and the energy level diagram shown in Fig. 1. In particular

$$\sigma_e(\lambda) = \sigma_a(\lambda)\frac{Z_L}{Z_u}\exp\left(-\frac{hc}{\lambda k_B T}\right)\exp\left(\frac{E_{UL}}{k_B T}\right) \quad (2.1)$$

$$Z_L = \sum_i \exp\left(-\frac{\Delta E_{Li}}{k_B T}\right) \quad (2.2)$$

$$Z_U = \sum_j \exp\left(-\frac{\Delta E_{Uj}}{k_B T}\right) \quad (2.3)$$

Fig. 1. Yb^{3+} energy levels derived from absorption and fluorescence spectra ($E_{UL} = 10288$ cm^{-1}).

where σ_a is the absorption cross section, h is Planck's constant, k_B is Boltzmann's constant, T is the absolute temperature in Kelvin, c is the vacuum speed of light, λ is the vacuum wavelength, E_{UL} is the energy difference between the lowest sublevels in the upper and lower manifolds, and ΔE_{Uj} (and ΔE_{Li}) is the energy differences between the Stark split sublevels and the lowest energy level in the upper manifold (lower manifold), respectively as given in Fig. 1.

As shown in Appendix A, (2.1) is derived based upon two assumptions. The first it that the population distribution between the Stark split sublevels in the upper and lower manifolds is given by Boltzmann statistics. This assumption will be valid provided the sublevel populations redistribute themselves to maintain thermal equilibrium on a time scale faster than any of the stimulated emission and absorption processes. This condition is reasonably met. The second assumption is that the linewidths, ΔE_{ij} (measured in units of energy), associated with the individual transitions between sublevel i in the lower manifold and a sublevel j in the upper manifold satisfies the condition

$$\Delta E_{ij} \ll k_B T \quad (2.4)$$

for all possible values of i and j, or equivalently

$$hc\frac{\Delta\lambda_{ij}}{\lambda_{ij}^2} \ll k_B T \quad (2.5)$$

where λ_{ij} is the vacuum wavelength of the transition between sublevels i and j in the lower and upper manifolds, respectively, and $\Delta\lambda_{ij}$ (wavelength units) is the corresponding linewidth of this transition. λ_{ij} is approximately 1 μm for all the individual Yb^{3+} transitions. Thus, (2.5) implies that $\Delta\lambda_{ij} \ll 21$ nm. This condition is met in Yb^{3+}-doped
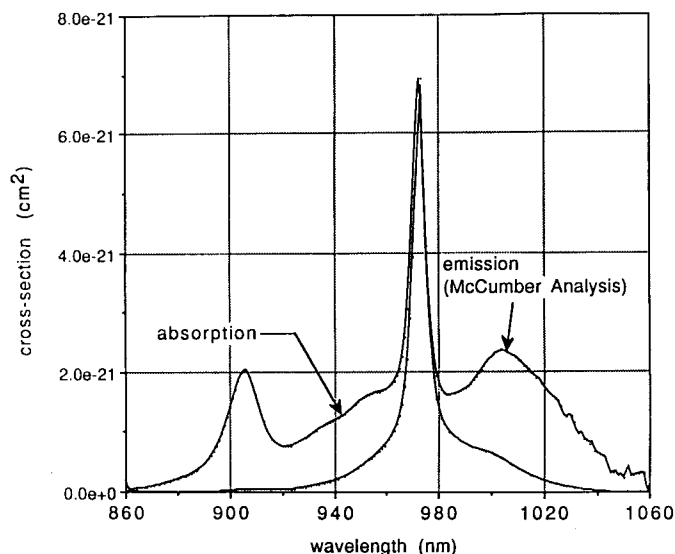
Fig. 2. Absorption and emission cross sections.

crystal hosts, but it is only approximately satisfied in glass, because inhomogeneous broadening can lead to rather wide transition linewidths. This fact, however, is often overlooked. Fig. 2 shows the measured absorption cross section of our glass taken with a Perkin–Elmer spectrophotometer and the emission cross section computed via the McCumber analysis described above. Using a 1-mm thick piece of the glass, the fluorescence spectra was also measured using an Ando optical spectrum analyzer. Data was collected for two different pump wavelengths, 909 and 940 nm. As Fig. 3 indicates, the shape of the measured fluorescence spectrum agrees approximately with the predictions of the McCumber analysis. Note that the fluorescence spectrum shows a slight dependence on the pump wavelength, because the energy levels of the Yb^{3+} vary somewhat from site-to-site in the glass [31]. Thus, at different pump wavelengths, ions at different sites in the glass are preferentially excited. The fluorescence time decay was also measured and is shown in Fig. 4 for a pump wavelength of 910 nm. The data indicates a nearly exponential decay with a $1/e$-lifetime of 1.3 ms. The primary contributions to the fluorescence signal are in the vicinity of 972 and 1005 nm. An examination of the energy level diagram of Fig. 1, indicates that both these wavelengths are produced by transitions originating from the lowest sublevel of the upper manifold and terminating on either of the two lowest sublevels of the lower manifold. The fact that both these transitions come from a common sublevel in the upper manifold is consistent with the observed time-dependence of the fluorescence decay, which is nearly exponential.

It is well known that the emission and absorption cross sections of rare earth-doped glasses depend on the glass composition, and data has been reported for a variety of Yb^{3+}-doped glasses [3], [15], [16], [30], [32]. Unfortunately the methods used to compute absolute values of emission cross sections in several of these papers are suspect, because they rely on the Landenburg–Fuchtbauer relationship [33], which is valid only for an ideal, two-level, homogeneous transition. The Landenburg–Fuchbauer relationship, which often appears

in many different equivalent forms, is given below

$$\frac{1}{\tau_{\text{rad}}} = \frac{8\pi}{3^*}\frac{n^2}{c^2}\int_0^\infty \nu^2\sigma_e(\nu)\,d\nu \qquad (2.6)$$

where τ_{rad} is the radiative lifetime of the transition, c is the vacuum speed of light, ν is frequency, n is the material refractive index associated with the polarization of the emission, and 3^* is a factor between 0 and 1, which accounts for polarization properties of the transition. In an isotropic material, such as glass, 3^* equals 1 [34]. The following general conclusions, however, may be drawn, from published data. First, silica fibers have their secondary emission peaks located in the vicinity of 1036 nm and fluorescence lifetimes on the order of 0.8 ms [3], [15]. Second, multicomponent silicate and borosilicate glasses tend to have their secondary emission peaks located closer to 1005 nm, lower emission cross sections, and considerably longer fluorescence lifetimes. Our data is consistent with the later observation.

It is widely known that the harmonic stretching vibration of OH ions in silica fibers is one of the principal loss mechanisms [35]. The principal OH absorption band is centered at 2.73 μm, and gives rise to additional absorption bands due to overtones and overtone combinations of the 2.73 μm stretch vibration. Only the 0.945 μm OH absorption bands lies in the wavelength range between 910 and 1100 nm. Our glass has a relatively low OH content, as indicated by a measured absorption coefficient of 1.4 cm^{-1} at a wavelength of 2.73 μm. In fused silica, the measured ratio of the strength of the OH absorption at 0.985 μm to that at 2.73 μm is approximately 10^{-4} [35]. Thus, using this ratio, we estimate an OH-induced loss in our glass of less than 6×10^{-4} dB/cm between 910 and 1100 nm, which is negligible.

III. DEVICE FABRICATION AND PERFORMANCE

The glass described in Table I was produced as a 2-lb melt and was subsequently cut and polished into $1'' \times 3'' \times 1$ mm thick pieces. A 1500 Å thick aluminum thin film was deposited on the glass surface and channel openings of various widths were subsequently formed using standard photolithographic techniques. Potassium ion exchange was performed by immersing the glass sample in a pure KNO_3 bath at 418 °C for 20 min. After the ion exchange step was completed, the aluminum mask was removed with aluminum etchant and the waveguide ends were polished. Prism coupling was performed on a section of the glass, where no aluminum mask had been deposited. This planar section supported two modes at 632.8 nm ($N_{\text{eff}} = 1.5174$ and $N_{\text{eff}} = 1.5148$), two modes at 830 nm ($N_{\text{eff}} = 1.5115$ and $N_{\text{eff}} = 1.5090$), and a single mode at 1300 nm ($N_{\text{eff}} = 1.5039$). The channel waveguides, corresponding to the 8-μm wide mask opening, generally supported a single mode at wavelengths in the vicinity of 1 μm. If due care was taken, however, a very weak second mode could sometimes be excited. With 1-μm light coupled into the waveguide by end-firing, the mode profile corresponding to the 8-μm wide mask opening, was measured using a microscope objective to image the end of the waveguide onto a CCD array. Special care was taken to
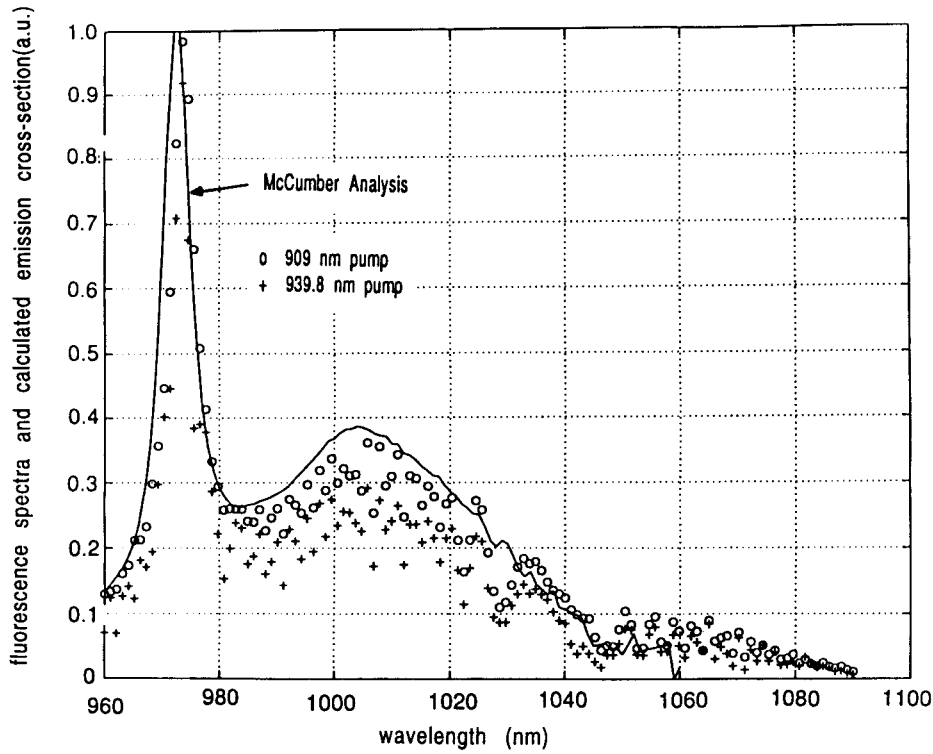
Fig. 3. Comparison of measured fluorescence spectra and emission cross section computed using McCumber analysis.
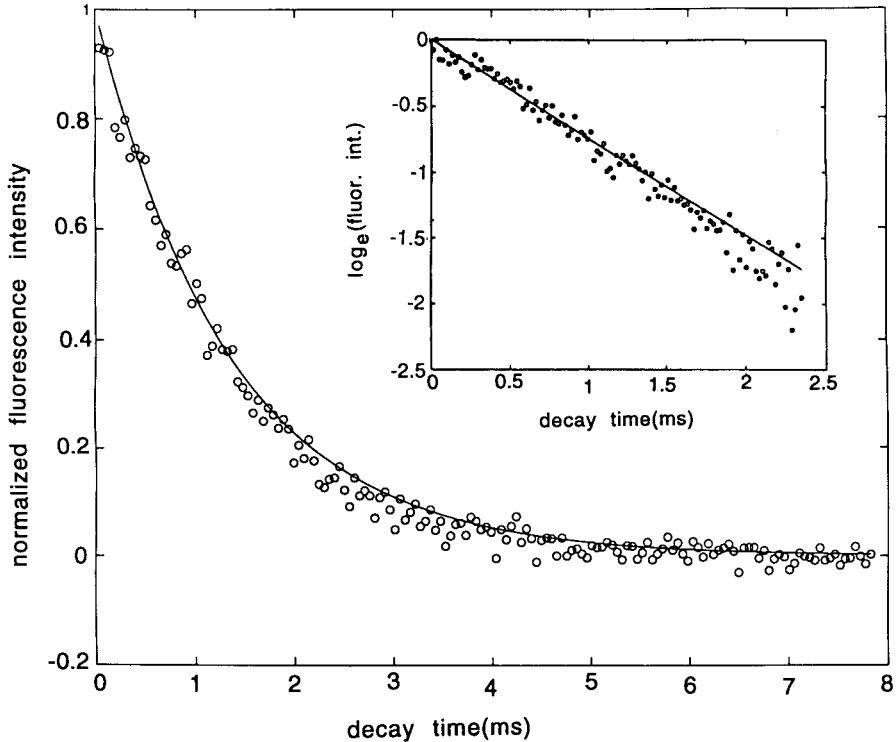

Fig. 4. Fluorescence decay. (o: measured values, ___ fit: $\exp(-t/1.3$ ms).

carefully calibrate the magnification of the imaging system and the linearity of the CCD array. The waveguide mode intensity contour profile is shown in Fig. 5. Using this mode profile data, the effective area, A_{eff}, of the waveguide (see (4.21)] was computed to be 16.5 μm^2 at a nominal wavelength of 1 μm. Waveguide propagation losses of 1.3 dB/cm (at a wavelength of 840 nm) and an end-fire coupling efficiency of 26% (at

a wavelength of 910 nm) were measured using the cutback method. It will be assumed that this propagation loss value is also approximately correct at wavelengths in the vicinity of 1 μm. The high propagation loss is likely due to surface roughness at the air/glass interface and/or scattering from inhomogenieties in the glass. With careful glass preparation, it should be possible to reduce this value to about 0.5 dB/cm.
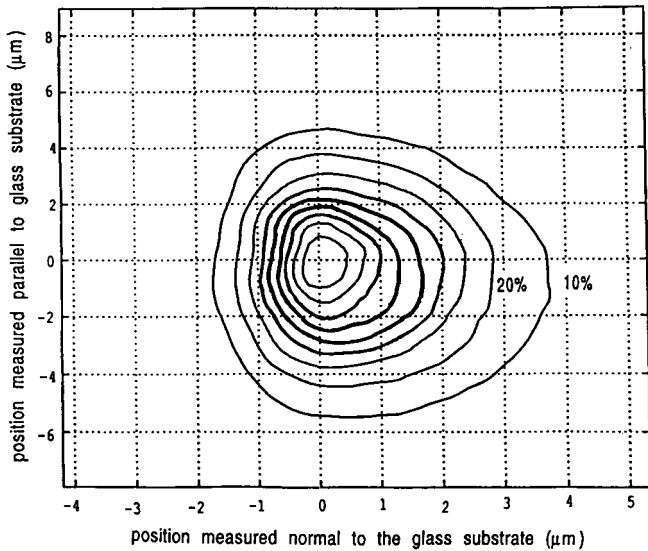
Fig. 5. Measured mode intensity contour plot. (Inner contour line is 90% of peak, while each additional line denotes a 10% decrease.)
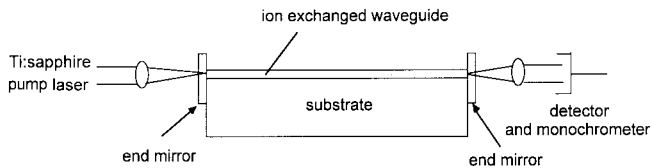

Fig. 6. Laser setup.

Broad-band multilayer dielectric mirror were deposited on thin microscope cover slips. These mirrors had reflectivities greater than 95% for the wavelength band between 1000 and 1100 nm and transmitted more than 90% of the incident light at 910 nm. Between 1020 and 1030 nm, the mirror reflectivities were approximately 96% (when the incident beam strikes the mirror from a medium with a refractive index of 1.5). The mirrors were attached to the waveguide ends using a transparent fluorinated liquid[1] with a refractive index of approximately 1.3 at a wavelenght of 589 nm. This index matching liquid filled the air gap between the mirrors and waveguide ends and thus suppressed etalon effects due to multiple reflections. The 2.2-cm long device was end-fire—pumped with transverse electric (TE)-polarized light by Ti : sapphire laser operating at 910 nm as shown in Fig. 6. The coupling efficiency was only about 26%, due to the poor mode profile of the Ti : sapphire laser pump beam. For this device, lasing occurred in the band between 1020 and 1030 nm, although some other devices fabricated in our laboratory lased at wavelengths as low as 1010 nm and as high as 1040 nm. The residual pump was separated form the lasing signal by a narrowband filter centered at 1 mm, which had a transmittance of 56% at 1020 nm. The waveguide laser had a threshold (launched pump power) and slope efficiency of approximately 45 mW and 5%, respectively, as shown in Fig. 7 when lasing occurred at 1020 nm. At pump powers exceeding 80 mW, the lasing output exhibited anamolous behavior, including multistability and hysteresis. These results are reported elsewhere [36]. Waveguide lasers were

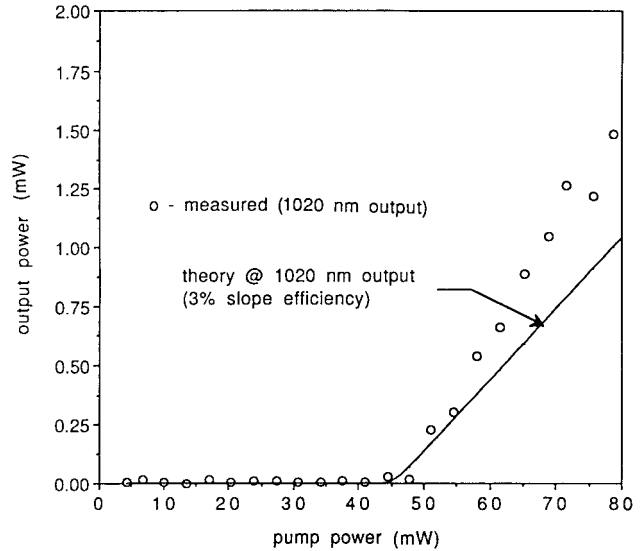[1] 3M Industrial Products Divison, St. Paul, MN.

Fig. 7. Output power versus pump power.

also demonstrated in our laboratory using Yb^{3+}-doped glass containing 6, rather than 12, weight precent Yb_2O_3 and in Yb^{3+}-doped glass waveguides fabricated by dilute silver in exchange. Detailed data on the performance of these devices, however, was not collected.

IV. DEVICE MODELING

The operation of the waveguide laser was modeled using a standard rate equation approach. The Yb^{3+} ion is treated as a two level system, with a population of n_1 ions/cm³ in the lower $^2F_{7/2}$ manifold and n_2 ions/cm³ in the upper manifold $^2F_{5/2}$. We will assume that the aggregate transition between the upper and lower manifolds can be modeled as being primarily homogeneously broadened. In addition, we will neglect spatial hole burning in our analysis. The pump and signal beam mode profiles are explicitly accounted for in our calculations. Invoking the above assumptions, the rate equations for the populations in the upper and lower manifolds can be written as

$$\frac{dn_2}{dt} = -W_{21}^{(p)}n_2 + W_{12}^{(p)}n_1 - W_{21}^{(s)}n_2$$
$$+ W_{12}^{(s)}n_1 - \frac{n_2}{\tau_{fl}} \quad (4.1)$$
$$n_1 + n_2 = N_{Yb} \quad (4.2)$$

where $W_{ij}(p,s)$ equals the stimulated emission rate (s⁻¹) from the ith to jth manifold induced by either the pump (p) or signal (s) beams, τ_{fl} is the fluorescence lifetime of the upper manifold, and N_{Yb} is the total Yb^{3+} concentration (ions/cm³) in the glass. The stimulated emission rates can be related to the total signal and pump beam intensities, I_s and I_p, respectively, by

$$W_{21}^{(s,p)} = \frac{\sigma_e^{(s,p)}I_{s,p}}{h\nu_{s,p}} \quad (4.3)$$

$$W_{12}^{(s,p)} = \frac{\sigma_a^{(s,p)}I_{s,p}}{h\nu_{s,p}} \quad (4.4)$$

The signal and pump beam saturation intensities, I_{ssat} and I_{psat}, respectively, are defined as

$$I_{ssat} = \frac{h\nu_s}{\sigma_a^{(s)}\tau_{fl}} \qquad (4.5)$$

$$I_{psat} = \frac{h\nu_p}{\sigma_a^{(p)}\tau_{fl}}. \qquad (4.6)$$

Setting dn_2/dt equal to zero, we can combine (4.1)–(4.6) to solve for the steady state population levels in the upper and lower manifolds. The results are

$$n_2 = \frac{\dfrac{I_p}{I_{psat}} + \dfrac{I_s}{I_{ssat}}}{1 + (1+\gamma_p)\dfrac{I_p}{I_{psat}} + (1+\gamma_s)\dfrac{I_s}{I_{ssat}}} N_{Yb} \qquad (4.7)$$

$$n_1 = \frac{\dfrac{I_p}{I_{psat}} + \dfrac{I_s}{I_{ssat}}}{1 + (1+\gamma_p)\dfrac{I_p}{I_{psat}} + (1+\gamma_s)\dfrac{I_s}{I_{ssat}}} N_{Yb} \qquad (4.8)$$

where

$$\gamma_{s,p} = \frac{\sigma_s^{(s,p)}}{\sigma_a^{(s,p)}}. \qquad (4.9)$$

We let z denote the coordinate axis along the direction of propagation in the waveguide and x, y the transverse coordinates in a plane normal to the propagation direction. The length of the waveguide will be denoted by L, and its ends will be assumed to be terminated by two mirrors with reflectivities R_1 and R_2, to form a cavity. The depletion of the pump beam and the growth of the signal beam, as they propagate along the z-axis ($z = 0$ is the launch pump point and mirror 1 is located here), can be described by the following set of differential equations:

$$\frac{dI_p(x,y,z)}{dz} = (-\sigma_a^{(p)}n_1(x,y,z) + \sigma_e^{(p)}n_2(x,y,z) - \alpha_p)$$
$$\cdot I_p(x,y,z) \qquad (4.10)$$

$$\frac{dI_s^{(+)}(x,y,z)}{dz} = (-\sigma_a^{(s)}n_1(x,y,z) + \sigma_e^{(s)}n_2(x,y,z) - \alpha_s)$$
$$\cdot I_s^{(+)}(x,y,z) \qquad (4.11)$$

$$\frac{dI_s^{(-)}(x,y,z)}{dz} = (\sigma_a^{(s)}n_1(x,y,z) - \sigma_e^{(s)}n_2(x,y,z) + \alpha_s)$$
$$\cdot I_s^{(-)}(x,y,z) \qquad (4.12)$$

where α_p and α_s are the waveguide propagation losses (cm^{-1}) for the pump and signal beams, respectively. $I_s^{(+)}$ and $I_s^{(-)}$ denote the intensities of the signal beam components propagating in the direction of increasing z (from $z = 0$ to $z = L$) and decreasing z (from $z = L$ to $z = 0$), respectively.

We now apply the standard Rigrod analysis [37]. It is easy to verify using (4.11) and (4.12) that

$$\frac{d(I_s^{(+)}(x,y,z)I_s^{(-)}(x,y,z))}{dz} = 0. \qquad (4.13)$$

Thus,

$$I_s^{(+)}(x,y,z)I_s^{(-)}(x,y,z) = \epsilon \qquad (4.14)$$

where ϵ is a constant. The presence of the cavity end mirrors require that the following conditions be met:

$$I_s^{(-)}(x,y,L) = R_2 I_s^{(+)}(x,y,L) \qquad (4.15)$$
$$I_s^{(+)}(x,y,0) = R_1 I_s^{(-)}(x,y,0). \qquad (4.16)$$

Combining (4.14)–(4.16) yields

$$I_s^{(-)}(x,y,z) = \frac{[I_s^{(+)}(x,y,0)]^2}{R_1 I_s^{(+)}(x,y,z)}. \qquad (4.17)$$

We will neglect spatial hole burning in this analysis, and therefore, we can write

$$I_s(x,y,z) = I_s^{(+)}(x,y,z) + I_s^{(-)}(x,y,z). \qquad (4.18)$$

Lasing requires that the round-trip gain equal the round-trip losses. Combining (4.14)–(4.16), it can be shown that the lasing condition is equivalent to

$$\frac{P_s^{(+)}(L)}{P_s^{(+)}(0)} = \frac{1}{\sqrt{R_1 R_2}} \qquad (4.19)$$

where $P_s^{(+)}(z)$ is the signal power propagating in the $+z$-direction at distance z measured along the waveguide from the pump launch point.

The signal and pump intensity mode profiles, $f_s(x,y)$ and $f_p(x,y)$, respectively, are given by

$$f_{s,p}(x,y) = \frac{I_{s,p}(x,y,z)}{\max_{x,y} I_{s,p}(x,y,z)} \qquad (4.20)$$

Since the pump and signal wavelengths lie within about 0.1 μm of one another, we will assume that both the pump and signal beams have identical mode profiles and experience the same propagation losses. The effective area, A_{eff}, of the mode is then given by (4.21).

$$A_{eff} = \int_{-\infty}^{\infty} \int_{-\infty}^{\infty} f(x,y)\, dx\, dy \qquad (4.21)$$

The pump and signal saturation powers can be expresses as follows:

$$P_{psat} = I_{psat}A_{eff} \qquad (4.22)$$
$$P_{ssat} = I_{ssat}A_{eff}. \qquad (4.23)$$

Integrating (4.10) and (4.11) over the the waveguide mode profiles yields

$$\frac{dP_p(z)}{dz} = \int_{-\infty}^{\infty} \int_{-\infty}^{\infty} (-\sigma_a^{(p)}n_1(x,y,z)$$
$$+ \sigma_e^{(p)}n_2(x,y,z) - \alpha)I_p(x,y,z)\, dx\, dy \quad (4.24)$$

$$\frac{dP_s^{(+)}(z)}{dz} = \int_{-\infty}^{\infty} \int_{-\infty}^{\infty} (-\sigma_a^{(s)}n_1(x,y,z)$$
$$+ \sigma_e^{(s)}n_2(x,y,z) - \alpha)I_s^{(+)}(x,y,z)\, dx\, dy$$
$$(4.25)$$

where $P_p(z)$ and $P_s^{(+)}(z)$ are the powers in the pump and signal beam (propagating in the $+z$-direction), respectively, expressed as a function of distance measured along the waveguide. Note that the emission and absorption cross sections

vanish outside of the Yb^{3+}-doped glass, and thus, strictly speaking, the terms

$$\sigma_{a,e}^{(s,p)}$$

in (4.24) and (4.25) have a spatial dependence. The mode intensities, however, decay very quickly in the air region above the glass surface, and therefore, this spatial dependence can be safely neglected. Combining (4.7)–(4.9) and (4.22)–(4.25) now yields

$$\frac{dP_p(z)}{dz} = -2\sigma_a^{(p)}N_{\text{Yb}}P_p(z)[e(z)A(d(z)) + B(d(z))]$$
$$+ 2\sigma_e^{(p)}N_{\text{Yb}}P_p(z)[d(z) - e(z)]A(d(z))$$
$$- \alpha P_p(z) \qquad (4.26)$$

$$\frac{dP_s^{(+)}(z)}{dz} = -2\sigma_a^{(s)}N_{\text{Yb}}P_s^{(+)}(z)[e(z)A(d(z)) + B(d(z))]$$
$$+ 2\sigma_e^{(s)}N_{\text{Yb}}P_s^{(+)}(z)[d(z) - e(z)]A(d(z))$$
$$- \alpha P_s^{(+)}(z) \qquad (4.27)$$

where

$$e(z) = \gamma_p \frac{P_p(z)}{P_{p\text{sat}}} + \gamma_s \frac{P_s(z)}{P_{s\text{sat}}} \qquad (4.28)$$

$$d(z) = (1 + \gamma_p)\frac{P_p(z)}{P_{p\text{sat}}} + (1 + \gamma_s)\frac{P_s(z)}{P_{s\text{sat}}} \qquad (4.29)$$

$$A(d) = \frac{1}{2A_{\text{eff}}} \int_{-\infty}^{\infty} \int_{-\infty}^{\infty} \frac{f^2(x,y)}{1 + df(x,y)} dx \, dy \qquad (4.30)$$

$$B(d) = \frac{1}{2A_{\text{eff}}} \int_{-\infty}^{\infty} \int_{-\infty}^{\infty} \frac{f(x,y)}{1 + df(x,y)} dx \, dy. \qquad (4.31)$$

The overlap mode integrals, given by (4.30) and (4.31), are plotted in Fig. 8 for three different intensity profiles $f(x,y)$: (1) a uniform intensity, (2) a two-dimensional, radially symmetric Gaussian intensity, and (3) the measured waveguide mode intensity described earlier. The dependence on d reflects how the values of the overlap integrals change as a function of the pump and the signal beam intensities. As one can see, a Gaussian mode profile yields overlap values which are nearly identical with those computed using measured mode profile data. On the other hand, the assumption of an uniform mode profile is seen to generate large errors. The computed lasing threshold and slope efficiency are very sensitive functions of the overlap integrals $A(d)$ and $B(d)$. For example, a uniform mode profile will yield a lasing threshold nearly a factor of three smaller and a slope efficiency approximately 30% larger than that calculated using the measured profiles shown in Fig. 5. Thus, the mode profiles must be carefully measured if the performance of the laser is to be accurately predicted.

Given the initial conditions, $P_p(0)$ and $P_s^{(+)}(0)$, the pair of coupled differential equations (4.26) and (4.27) can be solved numerically, by integrating them from $z = 0$ to $z = L$. With the launched pump power, $P_p(0)$, fixed, $P_s^{(+)}(0)$ is varied until the lasing condition given by (4.19) is satisfied. The corresponding output power, P_{out}, is then given by

$$P_{\text{out}} = (1 - R_2)P_s^{(+)}(L) + (1 - R_1)\frac{P_s^{(+)}(0)}{R_1}. \qquad (4.32)$$
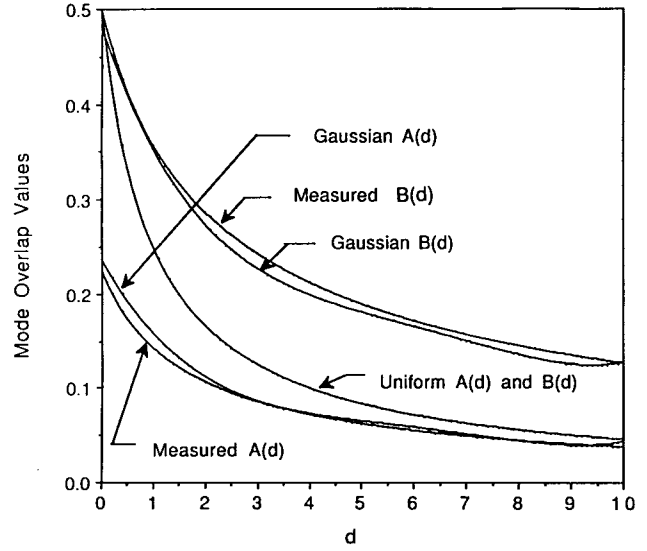

Fig. 8.   Spatial mode overlap integrals.

Using the above procedure, the theoretical curve of laser output power P_{out} versus launched pump power $P_p(0)$ was computed at a lasing wavelength of 1020 nm. The absorption and emission cross sections, the propagation losses, the fluorescence lifetime, and the mode profiles used in these calculations are those measured for our device and reported earlier in this paper. The results of our calculations are shown in Fig. 7, together with the experimentally measured values. Our modeling predicts a lasing threshold of 45 mW and a slope efficiency of 3%, while our measurements yield a threshold of about 45 mW and slope efficiency of approximately 5%. In Fig. 9 the predicted lasing threshold as a function of wavelength is also shown. This figure indicates that lasing anywhere from 1005 to 1030 nm might be expected when broadband end reflectors are used. Note that the calculated and measured lasing threshold values agree quite closely, while the slope efficiency predictions are not as accurate. We cannot easily explain the origin of this discrepancy. We do note, however, that the number of simplifying assumptions have been made in on our analysis, none of which are strictly correct. These assumptions include neglecting spatial hole burning, modeling the transition as purely homogeneously broadened, and assuming that the McCumber technique yields exact values for the emission cross section. Additional devices would need to be fabricated and tested, using a wide range of mirrors reflectivities, in order to completely assess the accuracy of our models.

No attempt was made to optimize the device reported in this paper. Careful glass selection should permit the waveguide propagation losses to be reduced to 0.5 dB/cm. Our model predicts a 30 mW threshold and a slope efficiency of 36% for a 1 cm long device ($R_1 = 100\%$ and $R_2 = 50\%$) lasing at 1020 nm with a propagation loss of 0.5 dB/cm. Provided there is sufficient gain, any desired lasing wavelength could be realized using either DBR or DFB gratings, in place of end-mirrors, as feedback elements. Efficient operation at wavelengths beyond 1040 nm, however, is problematic in our alkali-barium-silicate
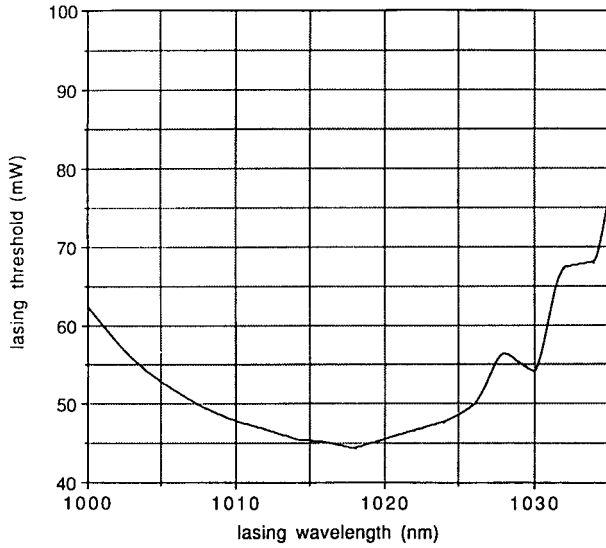
Fig. 9. Lasing threshold versus lasing wavelength.

glass due to the low emission cross section in this region. Alternate glasses, such as lithium-silicates may be preferable in this regard [32].

V. SUMMARY

A Yb^{3+}-doped glass, channel, waveguide laser has been demonstrated for the first time (to the best of our knowledge). The 2.2-cm long device was fabricated by potassium ion exchange in an alkali-barium-silicate glass containing 12 wt% Yb_2O_3. The device parameters, including absorption cross section, fluorescence lifetime, propagation loss, and mode profiles, were measured. Emission cross sections were computed from the measured absorption cross sections using the McCumber analysis. The device supported a single spatial mode and lased in the band between 1020 and 1030 nm when pumped with a Ti : sapphire laser operating at 910 nm. Using 96% end reflectors, a lasing threshold of approximately 50 mW (launched pump power) was measured with a slope efficiency of approximtately 5% at 1020 nm. A numerical model, based on a Rigrod analysis, was developed to predict laser performance. The model took into account the intensity profiles of the waveguide mode and accurately predicted the laser threshold. It performed less well, however, in explaining the observed slope efficiency. Our analysis indicates that a 1-cm long Yb_{3+}-doped glass, channel , waveguide laser operating at 1020 nm with a pump threshold of 30 mW and a slope efficiency of 36% should be realizable.

APPENDIX A
MCCUMBER ANALYSIS

Let f_{Uj} denote the fraction of the total upper manifold population which is located in sublevel j (see Fig. 1), and similarly f_{Li} equals the fraction of the total lower manifold population which is located in sublevel i. Assuming that thermal equilibrium is maintained in the Stark split sublevels, the relative populations in these levels is given by Boltzmann statistics. Therefore

$$f_{Uj} = \frac{\exp\left(-\frac{\Delta E_{Uj}}{k_B T}\right)}{Z_U} \qquad (A.1)$$

$$f_{Li} = \frac{\exp\left(-\frac{\Delta E_{Li}}{k_B T}\right)}{Z_L} \qquad (A.2)$$

where

$$Z_U = \sum_j \exp\left(-\frac{\Delta E_{Uj}}{k_B T}\right) \qquad (A.3)$$

$$Z_L = \sum_j \exp\left(-\frac{\Delta E_{Ui}}{k_B T}\right). \qquad (A.4)$$

The aggregate transition form the upper to lower manifold then has an effective emission cross section, σ_e, which can be written as the weighted average of the individual emission cross sections, $\sigma_e^{(ji)}$, from sublevel j to sublevel i

$$\sigma_e(\nu) = \frac{\sum_j \sum_i \exp\left(-\frac{\Delta E_{Uj}}{k_B T}\right)\sigma^{(ji)}_e(\nu)}{Z_U}. \qquad (A.5)$$

Similarly

$$\sigma_a(\nu) = \frac{\sum_i \sum_j \exp\left(-\frac{\Delta E_{Li}}{k_B T}\right)\sigma^{(ij)}_a(\nu)}{Z_L}. \qquad (A.6)$$

Combining (A.5) and (A.6) yields

$$\sigma_e(\nu) = \left[\sum_j \sum_i \frac{\exp\left(-\frac{\Delta E_{Li}}{k_B T}\right)}{Z_L}\sigma^{(ji)}_e(\nu)\right.$$
$$\left. \cdot \exp\left[\frac{(h\nu - E_{ji})}{k_B T}\right]\right] \frac{Z_L}{Z_U} \exp\left[\frac{E_{UL} - h\nu}{k_B T}\right]$$
$$\qquad (A.7)$$

where E_{UL} is the energy separation between the lower sublevels of the upper and lower manifolds, and E_{ji} is the energy separation between sublevels j and i in the upper and lower manifolds, respectively. Now if the linewidth of the emission cross section $\sigma_e^{(ji)}(n)$ is much less than $k_B T$, then the exponential term $\exp((h\nu - E_{ji})/k_B T)$ in (A.7) can be replaced by one. Combining (A.5)–(A.7) then yields

$$\sigma_e(\nu) = \sigma_a(\nu)\frac{Z_L}{Z_U} \exp\left[\frac{E_{UL} - h\nu}{k_B T}\right] \qquad (A.8)$$

which is known as the McCumber or the reciprocity relationship.

REFERENCES

[1] C. C. Robinson and J. T. Fournier, "Co-ordination of Yb^{3+} in phosphate, silicate, and germanate glasses," *J. Phys. Chem. Solids*, vol. 31, pp. 895–904, 1970.

[2] M. J. F. Digonnet, Ed., *Rare Earth Doped Fiber Lasers and Amplifiers*. New York: Marcel Dekker, 1993, pp. 35–38.

[3] H. M. Pask, R. J. Carman, D. C. Hanna, A. C. Tropper, C. J. Mackechnie, P. R. Barber, and J. M. Dawes, "Ytterbium-doped silica fiber lasers: Versatile sources for the 1–1.2 μm region," *J. Select. Topics Quantum Electron.*, vol. 1, pp. 1–13, 1995.

[4] V. Cautaerts, D. J. Richardson, R. Paschotta, and D. C. Hanna, "Stretched pulse Yb^{3+}: Silica fiber laser," *Opt. Lett.*, vol. 22, pp. 316–318, 1997.

[5] D. T. Walton, J. Nees, and G. Mourou, "Broad-bandwidth pulse amplification to the 10-mJ level in an Ytterbium-doped germanosilicate fiber," *Opt. Lett.*, vol. 21, pp. 1061–1063, 1996.

[6] Y. Ohishi, T. Kanamori, T. Kitagawa, S. Takahashi, E. Snitzer, and G. Sigel, "Pr^{3+}-doped fluoride fiber amplifier operating at 1.31 μm," *Opt. Lett.*, vol. 16, pp. 1747–1749, 1991.

[7] H. M. Pask, A. C. Tropper, D. C. Hanna, B. N. Samson, R. D. T. Lauder, P. R. Barber, L. Reekie, J. L. Archambault, S. T. Davey, and D. Szebesta, "Upconversion laser action in Pr^{3+}-doped ZBLAN fiber pumped by an Yb-doped silica fiber laser," in *Tech. Dig. Adv. Solid-State Lasers*, Salt Lake City, UT, , paper ATuD1-1, 1994, pp. 172–174.

[8] P. R. Barber, C. J. Mackechnie, R. D. T. Lauder, H. M. Pask, A. C. Tropper, D. C. Hanna, S. Butterworth, M. J. McCarthy, J.-L Archambault, and L. Reekie, "All solid-state blue room temperature thulium-doped upconversion fiber laser," in *Tech. Dig. Compact Blue-Green Lasers*, Salt Lake City, UT, , paper CFA3-1, 1994, pp. 68–70.

[9] C. S. Adams, J. Vorberg, and J. Mlynek, "Single-frequency operation of a diode-pumped lanthanum-neodymium-hexaaluminate laser by using a twisted-mode cavity," *Opt. Lett.*, vol. 18, pp. 420–422, 1993.

[10] K. A. Winick and G. L. Vossler, "Erbium:Ytterbium planar waveguide laser in ion-exchanged glass," in *Proc. SPIE: Rare-Earth-Doped Devices*, San Jose, CA., Feb. 10–11, 1997, vol. 2996, pp. 121–134.

[11] H. W. Entzel, H. W. Gandy, and R. J. Ginther, "Stimulated emission of infrared radiation from ytterbium activated silicate glass," *Appl. Opt.*, vol. 1, pp. 534–536, 1962.

[12] M. J. Weber, *Handbook of Laser Wavelengths*. Boca Raton, FL: CRC, 1999, pp. 141–162.

[13] M. J. Weber, *Handbook of Laser Wavelengths*. Boca Raton, FL: CRC, 1999, pp. 27–140.

[14] D. C. Hanna, R. M. Percival, I. R. Perry, R. G. Smart, P. J. Suni, J. E. Townsend, and A. C. Trooper, "Continuous-wave oscillation of a monomode ytterbium-doped fiber laser," *Electron. Lett.*, vol. 24, pp. 1111–1113, 1988.

[15] D. C. Hanna, R. M. Percival, I. R. Perry, R. G. Smart, P. J. Cuni, and A. C. Tropper, "An ytterbium-doped monomode fiber laser: Broadly tunable operation from 1.010–1.162 mm and three-level operation at 974 nm," *J. Mod. Opt.*, vol. 37, pp. 517–525, 1990.

[16] J. Y. Allain, M. Monerie, H. Poignant, and T. Georges, "High-efficiency ytterbium-doped fluoride fiber laser," *J. Non-Crystalline Solids*, vol. 161, pp. 270–273, 1993.

[17] J. Y. Allain, J. F. Bayon, M. Monerier, P. Bernage, and P. Niay, "Ytterbium-doped silica fiber laser with intracore Bragg gratings operating at 1.02 μm," *Electron. Lett.*, vol. 29, pp. 309–310, 1993.

[18] A. Asseh, H. Storoy, J. T. Kringlebotn, W. Margulis, B. Sahlgren, S. Sandgren, R. Stubbe, and G. Edwall, "10 cm Yb^{3+} DFB fiber laser with permanent phase shifted grating," *Electron. Lett.*, vol. 31, pp. 969–970, 1995.

[19] R. Paschotta, J. Nilsson, A. C. Tropper, and D. C. Hanna, "Ytterbium-doped fiber amplifiers," *J. Quantum Electron.*, vol. 33, pp. 1049–1056, 1997.

[20] J. P. Koplow, L. Goldberg, and D. A. V. Kliner, "Compact 1-W Yb-doped double-cladding fiber amplifier using V-groove side-pumping," *IEEE Photon. Technol. Lett.*, vol. 10, pp. 793–795, 1998.

[21] K. A. Winick, "Rare-earth-doped waveguide lasers in glass and $LiNbO_3$: A review," in *Proc. SPIE Rare-Earth Devices II*, vol. 3280, S. Honkanen and S. Jiang, Ed., San Jose, CA, Jan. 26–27, 1998, pp. 88–104.

[22] D. Pelenc, B. Chambaz, I. Chartier, B. Ferrand, C. Wyon, D. P. Shepherd, D. C. Hanna, A. C. Large, and A. C. Tropper, "High slope efficiency and low threshold in a diode-pumped epitaxially grown Yb:YAG waveguide laser," *Opt. Commun.*, vol. 115, p. 491, 1995.

[23] D. C. Hanna, J. K. Jones, A. C.. Large, D. P. Shepherd, A. C. Tropper, P. J. Chandler, M. J. Rodman, P. D. Townsend, and L. Zhang, "Quasi-three level 1.03 μm laser operation of a planar ion-implanted Yb:YAG waveguide," *Opt. Commun.*, vol. 99, pp. 211–215, 1996.

[24] M. Shimokozono, N. Sugimoto, A. Tate, Y. Katoh, M. Tanno, S. Fukuda, and T. Ryuoh, "Room-temperature operation of an Yb-doped $Gd_3Ga_5O_{12}$ buried channel waveguide laser at 1.025 μm wavelength," *Appl. Phys. Lett.*, vol. 68, p. 2177–2179, 1996.

[25] J. K. Jones, J. P. de Sandro, M. Hempstead, D. P. Shepherd, A. C. Large, A. C. Tropper, and J. S. Wilkinson, "Channel waveguide laser at 1 μm in Yb-indiffused $LiNbO_3$," *Opt. Lett.*, vol. 20, pp. 1477–1479, 1995.

[26] J. W. Arkwright, P. Elango, T. W. Whitbread, and G. R. Atkins, "Nonlinear phase changes at 1310 and 1545 nm observed far from resonance in diode pumped ytterbium doped fiber," *IEEE Photon. Technol. Lett.*, vol. 8, pp. 408–410, 1996.

[27] B. Wu, P. L. Chu, and J. Arkwright, "Ytterbium-doped silica slab waveguide with large nonlinearity," *Photon. Technol. Lett.*, vol. 7, pp. 1450–1452, 1995.

[28] C. C. Robinson and J. T. Fournier, "Coordination of Yb^{3+} in some inorganic glasses from optical absorption and emission studies," *Chem. Phys. Lett.*, vol. 3, pp. 517–519, 1969.

[29] D. E. McCumber, "Einstein relations connecting broadband emission and absorption spectra," *Phys. Rev.*, vol. 136, pp. A954–A957, 1964.

[30] X. Zou and H. Toratani, "Evaluation of spectroscopic properties of Yb^{3+}-doped glasses," *Phys. Rev. B*, vol. 52, pp. 889–897, 1995.

[31] S. Magne, M. Druetta, J. P. Goure, J. C. Thevenin, P. Ferdinand, and G. Monnom, "An ytterbium-doped monomode fiber laser: Amplified spontaneous emission, modeling of the gain and tunability in an external cavity," *J. Luminescence*, vol. 60 and 61, pp. 647–650, 1994.

[32] M. J. Weber, J. E. Lynch, D. H. Blackburn, and D. J. Cronin, "Dependence of the stimulated emission cross section of Yb^{3+} on host glass composition," *J. Quantum Electron.*, vol. QE-19, pp. 1600–1607, 1983.

[33] E. Desurvire, *Erbium-Doped Fiber Amplifiers*. New York: Wiley, 1994, pp. 244–270.

[34] A. Siegman, *Lasers*. Mill Valley, CA: University Science Books, 1986, pp. 150–153.

[35] P. Kaiser, A.R. Tynes, H. W. Astle, A. D. Pearson, W. G. French, R. E. Jaeger, and A. H. Cherin, "Spectral losses of unclad vitreous silica and soda-lime silicate fibers," *J. Opt. Soc. Amer.*, vol. 63, pp. 1141–1148, 1973.

[36] A. Kuditcher, M. P. Hehlen, C. M. Florea, K. W. Winick, and S.C. Rand, "Intrinsic multistability of Yb and Tm luminescence and stimulated emission in oxide glass," in *Proc. Conf. Lasers Electro-Optics (CLEO'99)*, Baltimore, MD, May 23–29, 1999, paper #QThG18, .

[37] A. Siegman, *Lasers*. Mill Valley, CA: University Science Books, 1986, pp. 485–490.

Catalin Florea (S'98) was born in Bucharest, Romania, in 1972. He received the B.S. degree in physics from Bucharest University, Romania, in 1995 and the M.S. degree in electrical engineering (optics) from the University of Michigan, Ann Arbor in 1999. He is currently pursuing the Ph.D. degree in applied physics at the University of Michigan.

In 1996, he joined the Integrated Optics Group at the University of Michigan. His research interests include rare-earth-doped glass and lithium niobate waveguide devices, periodically poled lithium niobate, photolithography for glass and lithium niobae, and gratings for DFB and DBR lasers.

Mr. Flores is a member of the IEEE Lasers and Electro-Optics Society (LEOS) and the Optical Society of America (OSA).

Kim A. Winick (S'77–M'80–SM'98) was born in New York City, NY, on July 27, 1954. He received the B.S. degree in electrical engineering from the Pennsylvania State University, University Park, in 1976, and the M.S. and Ph.D. degrees in electrical engineering from the University of Michigan, Ann Arbor, in 1977 and 1981, respectively. While at the University of Michigan, he held a National Science Foundation Graduate Fellowship.

From 1981 to 1988, he was a Technical Staff Member at the Massachusetts Institute of Technology Lincoln Laboratory, Cambridge, working on millimeter-wave and optical communication systems. In 1988, he joined the faculty of the Electrical Engineering and Computer Science Department at the University of Michigan, where he is currently an Associate Professor. His research interests are in the areas of glass and crystal integrated optics, information theory, and communications.

Dr. Winick is a member of the Optical Society of America (OSA).